Title
Southward Shift of Westerlies Intensifies the East Asian Early Summer Rainband Following El Niño

Journal
Geophysical Research Letters, 47(17)

ISSN
0094-8276

Authors
Kong, Wenwen
Chiang, John CH

Publication Date
2020-09-16

DOI
10.1029/2020gl088631

Peer reviewed

Southward shift of westerlies intensifies the East Asian early summer rainband following El Niño

Wenwen Kong[1] and John C. H. Chiang[1]

[1]Department of Geography and Berkeley Atmospheric Science Center, University of California, Berkeley, CA, USA

Corresponding author: Wenwen Kong (wenwen.kong@berkeley.edu)

Key Points

- Tropical tropospheric warming in summer following El Niño enhances the subtropical jet across the Tibetan Plateau.
- The resulting enhancement of extratropical northerlies downstream of the Plateau intensifies the June East Asian rainband.
- Mechanism for rainband enhancement following El Niño is similar to one proposed for rainband enhancement under warming.

Revised for Geophysical Research Letters

August 2020

Abstract

An intensification of East Asian rainfall usually occurs in summers following El Niño. We propose that this teleconnection is mediated via the westerlies impinging on the Tibetan Plateau, through El Niño's control on tropical tropospheric temperature. This is distinct from previous studies that attribute the El Niño's influence to changes in the Western Pacific subtropical anticyclone. The warming in the eastern equatorial Pacific leads to uniform warming of the entire tropical troposphere, which sharpens the temperature gradient between the tropics and the subtropics and shifts the westerlies southward. The westerlies impinge over the Tibetan Plateau for longer and, through interaction with the topography, induce intense and persistent extratropical northerlies downstream of the plateau that in turn intensifies the East Asian rainband. The rainband has previously been shown to intensify in a similar manner in a warming climate, suggesting that the El Niño response provides an analog for future changes.

Plain Language Summary

The East Asian summer monsoon (EASM) has profound impacts on agriculture and economics in the region. The intraseasonal evolution of the EASM undergoes substantial year-to-year variations, making its prediction a challenging task. El Niño events, a phenomenon that is associated with anomalous warming in the eastern equatorial Pacific, have been shown to cause more substantial summer rainfall and sometimes flooding over East Asia. Previous interpretations of the physical linkage between the El Niño and the EASM have focused on the role of the subtropical anticyclone in the western Pacific that drives the monsoonal flow into East Asia. Here we propose instead that it is the southward shift of the westerly winds impinging on the Tibetan Plateau that contributes to the intensification of the early summer rainband, particularly in June, through enhancing the plateau-modified flow downstream. Our results have implications for sub-seasonal to seasonal prediction of East Asian summer climate in response to the tropical Pacific sea surface temperature variations.

1. Introduction

The mei-yu-baiu-changma rainband (mei-yu, hereafter) is the primary intraseasonal rainfall stage of the East Asian summer monsoon (EASM), and tends to intensify during the decaying phase of El Niño episodes (Chang et al., 2000; Huang and Wu, 1989; Shen and Lau, 1995; Wang et al., 2012). Previous work has focused on the intensification of the western Pacific subtropical anticyclone as the underlying cause, through enhancing the water vapor transport into East Asia. Several interpretations have been proposed to explain the anticyclone intensification. One view argues that it occurs as a Rossby wave response (Gill, 1980) to the cold sea surface temperature (SST) anomalies over the western tropical Pacific during the developing phase of El Niño. This anomalous anticyclone persists into the summer following El Niño due to the positive feedback between surface wind, evaporation, and SST (wind-evaporation-SST feedback) (Wang and Zhang, 2002; Wang et al., 2000). An alternate view is the "Indian Ocean Capacitor" mechanism (Xie et al., 2009; Yang et al., 2007), which argues that the warming in the tropical Indian Ocean that peaks in the summer following an El Niño mediates the delayed effects of El Niño on East Asia summer climate. The Indian Ocean warming forces an equatorial Kelvin wave extending into the western Pacific, which then suppresses convection in the western North Pacific and establishes the anomalous anticyclone. Another school of thought suggests that the interaction of the annual cycle with ENSO during the latter's decaying phase (Stuecker et al., 2013, 2014) drives the anomalous lower tropospheric anticyclone over the western North Pacific (Zhang et al., 2015, 2016).

We explore an alternative interpretation of the teleconnection between El Niño and the East Asian summer rainband by focusing on the role of the upper-tropospheric westerlies. Recent studies (Chen and Bordoni, 2014a; Chiang et al., 2017; Kong and Chiang, 2019; Sampe and Xie, 2010) have shown that the westerlies impinging on the plateau is essential to the formation and maintenance of the East Asian rainband, from the spring rainfall over southeastern China (Park et al., 2012) to the pre-mei-yu and mei-yu stage during June and July (Chen and Bordoni, 2014b; Chiang et al., in press; Kong and Chiang, 2019; Molnar et al., 2010; Sampe and Xie, 2010). Moreover, Chiang et al. (2019) found that the East Asian rain band intensifies in June in the late 21st century under the RCP8.5 pathway emission scenario projections from the CESM large ensemble simulations (CESM-LENS, hereafter) (Kay et al., 2014). They attribute this to tropical tropospheric warming, which sharpens the meridional temperature contrast over the subtropics and shifts the westerly jet southward and enhances the westerlies impinging on the Tibetan Plateau.

By separating the contributions of the SST warming and the direct effect of greenhouse gases (GHG), they found that the SST warming dominates the pronounced tropical upper tropospheric warming while the direct GHG forcing counters the influence of SST warming. In a similar vein, Zhou et al. (2019) suggest that the projected warming over the eastern equatorial Pacific from the Climate Model Intercomparison Project Phase 5 (CMIP5) (Taylor et al., 2011) leads to southward displacement of westerlies and intensification of the early summer rainband. Both Zhou et al. (2019) and Chiang et al. (2019) point out a close connection between tropical oceanic warming, southward displacement of the jet, and intensification of East Asian summer rainband. However, both studies are based on model simulations, and the question remains whether the connection can be discerned from observations.

Here, El Niño provides a real-world test of the proposed linkage between tropical tropospheric temperature, westerlies, and the East Asian rainband. Warming in the eastern equatorial Pacific leads to uniform warming in the tropical troposphere (Chiang and Lintner, 2005; Chiang and Sobel, 2002), which sharpens the temperature gradient between the tropics and the subtropics, resulting in an anomalous southward displacement of the westerlies during the time when the westerlies undergo their seasonal northward migration across the Plateau. The westerlies thus linger over the Plateau latitiudes for longer, inducing intense and persistent extratropical northerlies downstream of the plateau that in turn leads to an intensified rainband. Note that the location and intensity of the East Asian westerlies usually covary with the tropospheric temperature gradient (Kuang and Zhang, 2005; Schiemann et al., 2009). The southward displacement of westerlies during summers following El Niño coexist with a strengthening of its intensity. We do not disentangle these two aspects of changes in this study. As will be shown later, we argue that the changes in the latitude of westerlies matter most (Kong and Chiang, 2019) for the East Asian summer rainband intensification.

2. Data and Methods

2.1 Rain Gauge and Reanalysis Data

Observed rain gauge data is from the APHRODITE daily product, APHRO_MA_025deg_V1101, at $0.25° \times 0.25°$ resolution (Yatagai et al., 2012). Historical SST is from the monthly $1° \times 1°$ Hadley Centre SST data set (HadISST1) (Rayner et al., 2003). We obtain daily and monthly zonal and meridional winds, geopotential height, air temperature, and specific humidity from the

NCEP/NCAR Reanalysis-1 dataset (Kalnay et al., 1996). We identify the ENSO phase from the winter of 1950/51 to 2014/15 and focus on the East Asian summer climate following El Niño peaks during 1951 to 2015. The Japanese 55-year Reanalysis (JRA-55) dataset (Ebita et al., 2011) is also employed to test the robustness of the results of the NCEP/NCAR dataset (see the supplementary material).

2.2 Model Simulations

We examined 300 years of output from the Large Ensemble 1° Pre-Industrial Fully Coupled control simulation with the Community Earth System Model version 1 (CESM1) (Hurrell et al., 2013), which has the same configuration as the CESM-LENS that is analyzed in Chiang et al. (2019). The case name of the simulation is b.e11.B1850C5CN.f09_g16.005, and model years 1901 to 2200 from the simulation were analyzed. This allows us to directly compare the East Asian response to El Niño in this run with the East Asian response to RCP8.5 forcing in Chiang et al. (2019).

2.3 Definition of the ENSO phase

We define the ENSO phase based on the Oceanic Niño Index (referred to as ONI). The ONI is defined as the 3-month running means of SST anomalies in the Niño 3.4 region $(5°N - 5°S, 120° - 170°W)$. We average the ONI over December-February (hereafter the DJF ONI), then detrend and standardize the resulting interannual timeseries (Lehner et al., 2016; McGraw and Barnes, 2016). An El Niño year is defined when the value exceeds +0.75, and a La Niña when this value is less than -0.75; all other years are defined as neutral ENSO. We identified 13 El Niño events, 16 La Niña events, and 36 neutral ENSO events from 1950/51 to 2014/15 (Table S1). We similarly identified 64 El Niño events, 73 La Niña events, and 163 neutral ENSO events from the CESM1 control simulation (not shown).

Past studies examining ENSO impacts usually compare responses contrasting the warm and cold phase of the ENSO. However, previous work suggests the response of the East Asian summer climate to El Niño and La Niña is asymmetric (Hardiman et al., 2018). We thus compare the East Asian climate in the summer following an El Niño with that during neutral summer and use the former minus the latter to denote their differences. We use the two-tailed student's t-test to show the statistical significance of our results.

3. Observed responses during the summer following El Niño

The seasonal evolution of the East Asian summer monsoon rainfall in summers following an El Niño resembles those for neutral summers (Figure 1a), except for a pronounced rainfall intensification from June to mid-July over the south to central East China (Figures 1b, 1g, 1h). Relative to the amount received in neutral summer years, the intensification of June to July precipitation over south-central East China exceeds 1.5 mm/day (Figure 1b). In climatology, the pre-mei-yu season starts in mid-May over southeastern China, while the mei-yu season starts in mid-to-late June when the rainband jumps northward to central-eastern China and ends in late July (Ding and Chan, 2005). The timing of the rainfall intensification co-incides with the pre-mei-yu and mei-yu stages, and both rain stages feature banded precipitation (Chiang et al., 2020; Day et al., 2018). Here, the "banded" rainfall is associated with large-scale convergence, while the "local" rainfall is driven by local buoyancy or topography (Day et al., 2018). Indeed, partitioning of the banded and local rainfall suggests that the rainfall intensification primarily arises from the banded precipitation, suggesting an enhancement in the large-scale convergence over the region during summers following El Niño (Day et al., 2018; see Text S1 and Figures S1-S2). We also examined the NCEP/NCAR-1 precipitation, which includes values over the ocean and is physically consistent with the NCEP/NCAR-1 circulation field. Intensification of the NCEP/NCAR-1 precipitation is weaker than the APHRODITE, and their spatial patterns differ; this difference may arise from the fact that the NCEP/NCAR-1 does not assimilate observed precipitation and thus is an entirely modeled quantity. That said, the NCEP/NCAR-1 response also features rainfall intensification concentrating over south-central East China from June to July (Figure S3). Similar analysis with the CMAP (CPC Merged Analysis of Precipitation) dataset (Xie and Arkin, 1997) further supports that the rainband intensification is a robust response during summers following El Niño, and that this intensification is strongest in June (Figure S4).

In the following subsections, we will discuss the physical cause of the June and July intensification separately. In particular, we will show that the southward shift of westerlies is the reason for the June rainband intensification over East Asia.

3.1 Southward shift of westerlies intensifies the rainband in June

There is a delayed northward migration of the westerlies across the Tibetan Plateau in June and July following an El Niño (Figures 1c-d). Since the climatological westerlies reach the northern edge of the plateau (~$40°N$) in June, this delayed migration implies that the westerlies linger longer over the Plateau latitudes (Figures 2a-c). As suggested by Kong and Chiang (2019) and Chiang et al. (in press), this will lead to enhanced flow-orography interaction between the westerlies and the plateau, resulting in stronger extratropical northerlies downstream of the plateau; this is indeed observed in the 500 mb meridional wind response following an El Niño (Figures 1e-f and Figures 2d-f).

The synchronous changes in the June rainfall, westerlies, and northerlies of East Asia resemble the results of Chiang et al. (2019), who found similar responses of East Asian summer climate at the end of the 21st century in the RCP8.5 as simulated by the CESM-LENS. They show that the root cause of the projected intensification of East Asian early summer rainband is the warmer tropical tropospheric temperatures resulting from tropical oceanic warming, that in turn strengthens the subtropical jet impinging on the Tibetan Plateau. A similar response occurs here, except that in our case the tropical tropospheric warming is driven by El Niño. In agreement with previous findings (Seager et al., 2003), there is a tropics-wide warming of the tropical troposphere and cooling in the mid-high latitudes over the Eurasian continent. The atmospheric temperature gradient between the tropics and the extratropics thus sharpens over Eurasia (Figure 2h and Figure S5a), and the westerly jet shifts to the south of its climatological position (Figures 2b-c). Consistent with the tropics-wide tropospheric warming, there is basinwide warming of the tropical SST in both the tropical Indian and Atlantic Oceans (Figure 2g).

By using a vertically integrated moisture budget analysis, our recent studies find that enhancement of extratropical northerlies and the resultant strengthening of meridional wind convergence is key to intensify the East Asian rainband (Chiang et al., 2019; Kong and Chiang, 2019). Here, we also employed moisture budget analysis for the summers following El Niño and found that changes in the meridional wind convergence appear to be the root cause of the June rainband intensification (Text S2 and Figure S6). This is in agreement with the cause of the late 21st century rainband intensification as diagnosed in Chiang et al. (2019). Finally, the June rainfall intensification over the western North Pacific also results from enhanced meridional moisture flux convergence (Figure S3 and Figure S6g), implying that the rainfall intensification over the ocean is part of a large-scale rainband intensification.

3.2 Rainband intensification in July

The proposed bridging effect by the westerlies between El Niño and the East Asian rainband does not appear to operate for July. It is because the tropospheric temperature response to El Niño gradually damps following an El Niño. Compared to June, the temperature contrast between the tropics and the subtropics is considerably reduced in July (Figure S5b). Thus, though the westerlies over the Plateau latitudes also show a southward shift during July following El Niño (Figure 1d), this perturbation is not strong enough to strengthen the orographic downstream northerlies as seen in June (cf. Figures S7e-f and Figures 2e-f). The results discussed below do not change even when we focus our analysis from early to mid-July (not shown), the interval when July rainfall intensification occurs (Figure 1b).

We attribute the rainfall intensification in July to an enhancement of the western Pacific subtropical high, which intensifies the monsoonal southwesterlies. Indeed, the moisture budget analysis in July suggests that the zonal wind convergence from anomalous westerlies (not shown) and the meridional wind convergence from anomalous southerlies (Figures S7f-g) dominate the moisture flux convergence in central East China. Figures 3a-d present the lower tropospheric winds and the mid-tropospheric eddy geopotential height. The eddy geopotential height is a measure of the western Pacific subtropical high, which by nature is a planetary wave (Rodwell and Hoskins, 2001). We calculate the eddy geopotential height by deviation of geopotential height from the regional averaged over $0° - 40°N, 180°W - 180°E$, which is recommended by He et al. (2015) as a more reasonable measure of the western Pacific subtropical high than removing the zonal mean at each latitude. In June, cyclonic circulation and northerly anomalies dominate central-northern East China, while the intensification of the subtropical high is confined over the South China sea. In July, however, the enhancement of extratropical northerlies disappears and the anticyclonic anomalies dominate south to central China.

Taken together, the above observational analysis suggests that following El Niño, the East Asian summer rainband intensifies from June to July, with the most of the intensification occuring in June. For the June rainfall intensification, we did not find evidence supporting previously suggested contributions from the western Pacific subtropical high. Instead, we argue that the June rainband intensification results from enhanced extratropical northerlies, which is induced by the flow-orography interaction due to a southward shift of westerlies (Kong and Chiang, 2019). The effects of perturbation in westerlies on the rainband disappear in July, and during this time the enhancement of the western Pacific subtropical high presumably comes into play. We repeated the above ananlysis with the JRA-55 dataset (Ebita et al., 2011) and found similar results (Text S3 and Figs. S13-17).

4. Results from CESM1 pre-industrial control simulation

We further examine the El Niño teleconnection to East Asia in a CESM1 pre-industrial control simulation. This allows for a considerably larger sample of El Niño events to assess statistical significance, and furthermore the changes inferred here can be directly compared to the CESM-LENS results in Chiang et al. (2019) given that the same model is used.

Similar to the observations, the East Asian rainband in the summer following El Niño in the CESM1 control run undergoes intensification in June and July (Figures 4a-b and g-h). This intensification is accompanied by a southward shift of westerlies over the Plateau, and enhanced extratropical northerlies downstream of it (Figures 4c-f and Figures S9-S10). The strong southward displacement in the westerlies following El Niño episodes persists into July in the model simulations, which differs from results in section 3. As a result, the extratropical northerly anomalies are strong in both months, and lead to intensified rainbands in both June and July. We think that the persistence of the signal into July arises from the simulated El Niño magnitude being stronger and the decay from peak El Niño being more gradual than the observations (Figure S11), resulting in a more persistent tropical SST and tropospheric warming in the summer following El Niño (Figure S12). The enhancement of both northerlies and southerlies results in enhancement of large-scale frontal convergence and explains why the July rainband intensification is so pronounced in the CESM1 simulation.

5. Summary and Discussion

We reveal a teleconnection mechanism between El Niño and the East Asian early summer rainband through the former's control on the westerlies impinging on the Tibetan Plateau. Both observational analysis and model simulations show that westerlies during the summer following

El Niño are shifted southward, prolonging the westerlies' impinging on the Plateau. The resulting orographic forcing leads to a strengthening of the northerlies downstream of the Tibetan Plateau, and intensification of rainfall over south to central East China. This mechanism is similar to ones proposed in recent studies that show a dynamical linkage between the latitude of westerlies impinging on the plateau and the timing and duration of East Asian summer rainfall (Chiang et al., 2020; Kong and Chiang, 2019). In this instance, the southward shift of westerlies results from a sharpening of meridional temperature contrast at the subtropics, arising from a warming of the tropical troposphere in response to the warming in the eastern equatorial Pacific.

The similarity in the mechanism of rainband intensification found here, with that found in Chiang et al. (2019) for the intensification in the late 21st century from RCP 8.5 simulations, suggests that observed East Asian early summer rainband response to El Niño can be viewed as a modern-day analog to projected rainband changes under global warming. If this is indeed the case, then these observed instances can potentially be used to provide guidance on the nature of the future East Asian rainfall changes, in particular with changes to rainfall extremes. Notably, the CESM-LENS projections suggest that East Asian summer rainfall extremes will double in the late 21st century (Chiang et al., 2019).

Recent studies suggest that ENSO possesses rich diversity in the structure and warming magnitude of SST and remote impacts (Capotondi et al., 2014; Johnson, 2013; Takahashi et al., 2011). The relationship of our proposed mechanism to the type of ENSO event remains to be explored. An additional question worth exploring is whether the asymmetric response of East Asian summer rainfall to El Niño and La Niña (Hardiman et al., 2018) arises from different responses of the westerlies to positive versus negative SST anomalies in the eastern equatorial Pacific. Another problem that we leave for future study is how our mechanism relates to previous studies that tie the teleconnection to the role of the western Pacific subtropical high. One intriguing question in particular is how the enhancement of the western Pacific subtropical high and the northward shift of westerly jet are dynamically linked.

Acknowledgments, Samples, and Data

This work was supported by the National Science Foundation Grant AGS-1405479. We thank the editor Dr. Alessandra Giannini and two anonymous reviewers for their careful reviews and insightful comments. W.K. thanks David Battisti for helpful conversations. We thank Jesse Day for sharing the banded and non-banded rainfall in APHRODITE (https://figshare.com/projects/Data_and_code_for_Changing_character_of_rainfall_in_eastern_China_1951-2007_/28563). We obtained the NCEP-NCAR1 dataset from https://www.esrl.noaa.gov/psd/data/gridded/data.ncep.reanalysis.html. The NCEP-NCAR 1 precipitation rate is downloaded from the IRI/LDEO Climate Data Library. The CMAP Precipitation data is provided by the NOAA/OAR/ESRL PSL, Boulder, Colorado, USA, from their website at https://psl.noaa.gov/data/gridded/data.cmap.html. The JRA-55 dataset can be obtained from Research Data Archive at the National Center for Atmosphereic Research, Computational and Information Systems Laboratory (https://climatedataguide.ucar.edu/climate-data/jra-55). We thank the APHRODITE's Water Resources (https://www.chikyu.ac.jp/precip/english/) for providing the APHRODITE dataset. The HadISST dataset is obtained from https://www.metoffice.gov.uk/hadobs/hadisst/data/download.html. We thank the CESM Large Ensemble Community Project for making their model simulations publicly available at http://www.cesm.ucar.edu/projects/community-projects/LENS/data-sets.html. We would like to acknowledge high-performance computing support from Cheyenne (doi:10.5065/D6RX99HX) provided by NCAR's Computational and Information Systems Laboratory, sponsored by the National Science Foundation.

References

Capotondi, A., Wittenberg, A.T., Newman, M., Di Lorenzo, E., Yu, J.-Y., Braconnot, P., Cole, J., Dewitte, B., Giese, B., Guilyardi, E., et al. (2014). Understanding ENSO Diversity. Bull. Amer. Meteor. Soc. *96*, 921–938.

Chang, C.-P., Zhang, Y., and Li, T. (2000). Interannual and Interdecadal Variations of the East Asian Summer Monsoon and Tropical Pacific SSTs. Part I: Roles of the Subtropical Ridge. J. Climate *13*, 4310–4325.

Chen, J., and Bordoni, S. (2014a). Intermodel spread of East Asian summer monsoon simulations in CMIP5. Geophys. Res. Lett. *41*, 1314–1321.

Chen, J., and Bordoni, S. (2014b). Orographic Effects of the Tibetan Plateau on the East Asian Summer Monsoon: An Energetic Perspective. J. Climate *27*, 3052–3072.

Chiang, J.C.H., and Lintner, B.R. (2005). Mechanisms of Remote Tropical Surface Warming during El Niño. J. Climate *18*, 4130–4149.

Chiang, J.C.H., and Sobel, A.H. (2002). Tropical Tropospheric Temperature Variations Caused by ENSO and Their Influence on the Remote Tropical Climate. J. Climate *15*, 2616–2631.

Chiang, J.C.H., Swenson, L.M., and Kong, W. (2017). Role of seasonal transitions and the westerlies in the interannual variability of the East Asian summer monsoon precipitation. Geophys. Res. Lett. *44*, 2017GL072739.

Chiang, J.C.H., Fischer, J., Kong, W., and Herman, M.J. (2019). Intensification of the Pre-Meiyu Rainband in the Late 21st Century. Geophysical Research Letters *46*, 7536–7545.

Chiang, J.C.H., Kong, W., Wu, C.-H., and Battisti, D.S. (2020). Origins of the East Asian Summer Monsoon Seasonality. In Press for Journal of Climate.

Day, J.A., Fung, I., and Liu, W. (2018). Changing character of rainfall in eastern China, 1951–2007. PNAS 201715386.

Ding, Y., and Chan, J.C.L. (2005). The East Asian summer monsoon: an overview. Meteorol. Atmos. Phys. *89*, 117–142.

Ebita, A., Kobayashi, S., Ota, Y., Moriya, M., Kumabe, R., Onogi, K., Harada, Y., Yasui, S., Miyaoka, K., Takahashi, K., et al. (2011). The Japanese 55-year Reanalysis "JRA-55": An Interim Report. SOLA *7*, 149–152.

Gill, A.E. (1980). Some simple solutions for heat-induced tropical circulation. Q.J.R. Meteorol. Soc. *106*, 447–462.

Hardiman, S.C., Dunstone, N.J., Scaife, A.A., Bett, P.E., Li, C., Lu, B., Ren, H.-L., Smith, D.M., and Stephan, C.C. (2018). The asymmetric response of Yangtze river basin summer rainfall to El Niño/La Niña. Environ. Res. Lett. *13*, 024015.

Huang, R., and Wu, Y. (1989). The influence of ENSO on the summer climate change in China and its mechanism. Adv. Atmos. Sci. *6*, 21–32.

Hurrell, J.W., Holland, M.M., Gent, P.R., Ghan, S., Kay, J.E., Kushner, P.J., Lamarque, J.-F., Large, W.G., Lawrence, D., Lindsay, K., et al. (2013). The Community Earth System Model: A Framework for Collaborative Research. Bull. Amer. Meteor. Soc. *94*, 1339–1360.

Johnson, N.C. (2013). How Many ENSO Flavors Can We Distinguish?*. J. Climate *26*, 4816–4827.

Kalnay, E., Kanamitsu, M., Kistler, R., Collins, W., Deaven, D., Gandin, L., Iredell, M., Saha, S., White, G., Woollen, J., et al. (1996). The NCEP/NCAR 40-Year Reanalysis Project. Bull. Amer. Meteor. Soc. *77*, 437–471.

Kay, J.E., Deser, C., Phillips, A., Mai, A., Hannay, C., Strand, G., Arblaster, J.M., Bates, S.C., Danabasoglu, G., Edwards, J., et al. (2014). The Community Earth System Model (CESM) Large Ensemble Project: A Community Resource for Studying Climate Change in the Presence of Internal Climate Variability. Bull. Amer. Meteor. Soc. *96*, 1333–1349.

Kong, W., and Chiang, J.C.H. (2019). Interaction of the Westerlies with the Tibetan Plateau in Determining the Mei-Yu Termination. J. Climate *33*, 339–363.

Kuang, X., and Zhang, Y. (2005). Seasonal variation of the East Asian Subtropical Westerly Jet and its association with the heating field over East Asia. Adv. Atmos. Sci. *22*, 831–840.

Lehner, F., Schurer, A.P., Hegerl, G.C., Deser, C., and Frölicher, T.L. (2016). The importance of ENSO phase during volcanic eruptions for detection and attribution. Geophysical Research Letters *43*, 2851–2858.

McGraw, M.C., and Barnes, E.A. (2016). Seasonal Sensitivity of the Eddy-Driven Jet to Tropospheric Heating in an Idealized AGCM. J. Climate *29*, 5223–5240.

Molnar, P., Boos, W.R., and Battisti, D.S. (2010). Orographic Controls on Climate and Paleoclimate of Asia: Thermal and Mechanical Roles for the Tibetan Plateau. Annual Review of Earth and Planetary Sciences *38*, 77–102.

Park, H.-S., Chiang, J.C.H., and Bordoni, S. (2012). The Mechanical Impact of the Tibetan Plateau on the Seasonal Evolution of the South Asian Monsoon. Journal of Climate *25*, 2394–2407.

Rayner, N.A., Parker, D.E., Horton, E.B., Folland, C.K., Alexander, L.V., Rowell, D.P., Kent, E.C., and Kaplan, A. (2003). Global analyses of sea surface temperature, sea ice, and night marine air temperature since the late nineteenth century. Journal of Geophysical Research: Atmospheres *108*.

Rodwell, M.J., and Hoskins, B.J. (2001). Subtropical Anticyclones and Summer Monsoons. J. Climate *14*, 3192–3211.

Sampe, T., and Xie, S.-P. (2010). Large-Scale Dynamics of the Meiyu-Baiu Rainband: Environmental Forcing by the Westerly Jet*. Journal of Climate *23*, 113–134.

Schiemann, R., Lüthi, D., and Schär, C. (2009). Seasonality and Interannual Variability of the Westerly Jet in the Tibetan Plateau Region*. Journal of Climate *22*, 2940–2957.

Seager, R., Harnik, N., Kushnir, Y., Robinson, W., and Miller, J. (2003). Mechanisms of Hemispherically Symmetric Climate Variability. J. Climate *16*, 2960–2978.

Shen, S., and Lau, K.-M. (1995). Biennial Oscillation Associated with the East Asian Summer Monsoon and Tropical Sea Surface Temperatures. Journal of the Meteorological Society of Japan. Ser. II *73*, 105–124.

Stuecker, M.F., Timmermann, A., Jin, F.-F., McGregor, S., and Ren, H.-L. (2013). A combination mode of the annual cycle and the El Niño/Southern Oscillation. Nature Geoscience *6*, 540–544.

Stuecker, M.F., Jin, F.-F., Timmermann, A., and McGregor, S. (2014). Combination Mode Dynamics of the Anomalous Northwest Pacific Anticyclone. J. Climate *28*, 1093–1111.

Takahashi, K., Montecinos, A., Goubanova, K., and Dewitte, B. (2011). ENSO regimes: Reinterpreting the canonical and Modoki El Niño. Geophysical Research Letters *38*.

Taylor, K.E., Stouffer, R.J., and Meehl, G.A. (2011). An Overview of CMIP5 and the Experiment Design. Bull. Amer. Meteor. Soc. *93*, 485–498.

Wang, B., and Zhang, Q. (2002). Pacific–East Asian Teleconnection. Part II: How the Philippine Sea Anomalous Anticyclone is Established during El Niño Development. J. Climate *15*, 3252–3265.

Wang, B., Wu, R., and Fu, X. (2000). Pacific–East Asian Teleconnection: How Does ENSO Affect East Asian Climate? J. Climate *13*, 1517–1536.

Wang, X., Wang, D., Zhou, W., and Li, C. (2012). Interdecadal modulation of the influence of La Niña events on mei-yu rainfall over the Yangtze River valley. Adv. Atmos. Sci. *29*, 157–168.

Xie, P., and Arkin, P.A. (1997). Global Precipitation: A 17-Year Monthly Analysis Based on Gauge Observations, Satellite Estimates, and Numerical Model Outputs. Bull. Amer. Meteor. Soc. *78*, 2539–2558.

Xie, S.-P., Hu, K., Hafner, J., Tokinaga, H., Du, Y., Huang, G., and Sampe, T. (2009). Indian Ocean Capacitor Effect on Indo–Western Pacific Climate during the Summer following El Niño. J. Climate *22*, 730–747.

Yang, J., Liu, Q., Xie, S.-P., Liu, Z., and Wu, L. (2007). Impact of the Indian Ocean SST basin mode on the Asian summer monsoon. Geophysical Research Letters *34*.

Yatagai, A., Kamiguchi, K., Arakawa, O., Hamada, A., Yasutomi, N., and Kitoh, A. (2012). APHRODITE: Constructing a Long-Term Daily Gridded Precipitation Dataset for Asia Based on a Dense Network of Rain Gauges. Bull. Amer. Meteor. Soc. *93*, 1401–1415.

Zhang, W., Li, H., Stuecker, M.F., Jin, F.-F., and Turner, A.G. (2015). A New Understanding of El Niño's Impact over East Asia: Dominance of the ENSO Combination Mode. J. Climate *29*, 4347–4359.

Zhang, W., Jin, F.-F., Stuecker, M.F., Wittenberg, A.T., Timmermann, A., Ren, H.-L., Kug, J.-S., Cai, W., and Cane, M. (2016). Unraveling El Niño's impact on the East Asian Monsoon and Yangtze River summer flooding. Geophys. Res. Lett. *43*, 2016GL071190.

Zhou, W., Xie, S.-P., and Yang, D. (2019). Enhanced equatorial warming causes deep-tropical contraction and subtropical monsoon shift. Nat. Clim. Chang. *9*, 834–839.

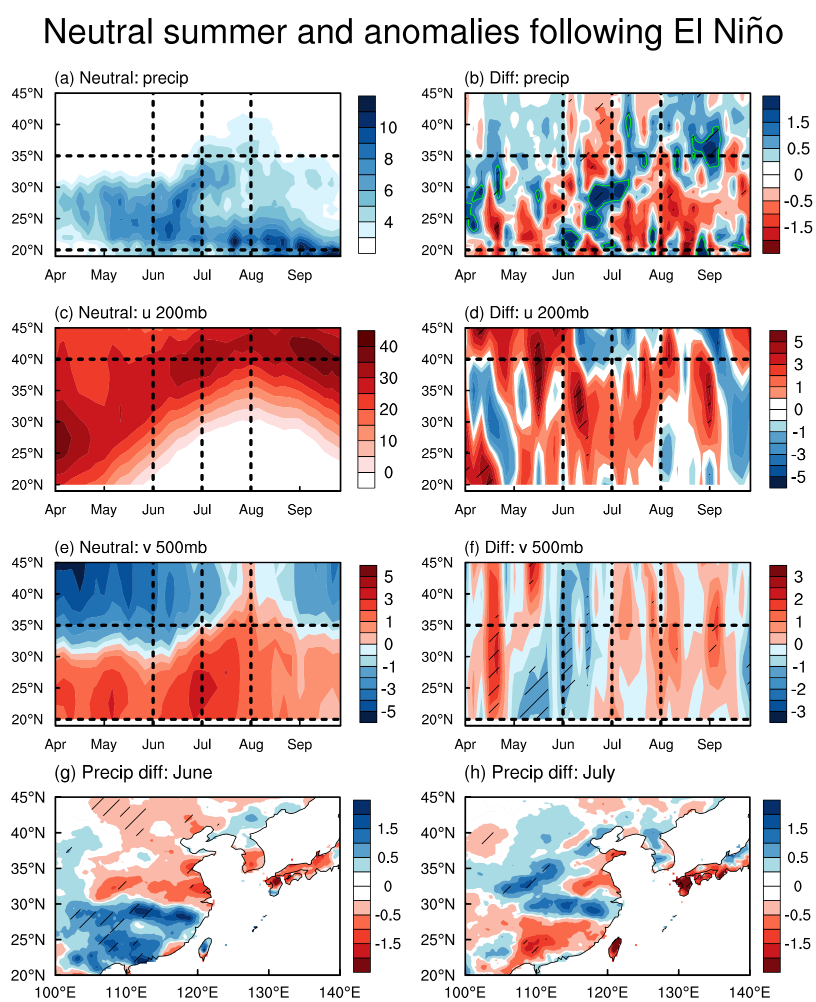

Figure 1. APHRODITE rain gauge data, NCEP1 200mb zonal wind, and 500mb meridional wind in decaying phase of El Niño events and the neutral summers. (a)-(b) Hovmöller diagram of rainfall over East China $(105°E - 120°E)$ for (a) neutral summers, and (b) the difference between the two categories (El Niño minus neutral), where the green solid contour highlights precipitation anomalies exceeding 1.5 mm/day. (c)-(d) Hovmöller diagram of 200mb zonal wind averaged in the Tibetan Plateau region $(80°E - 100°E)$ for (c) neutral summers, and (d) difference between the two categories. (e)-(f) Hovmöller diagram of 500mb meridional wind averaged over East China $(105°E - 120°E)$ for (e) neutral summers, and (f) difference between the two categories. (g)-(h) Precipitation of El Niño decaying phase minus neutral summers in (g) June and (h) July. Unit: mm/day for (a)-(b), (g)-(h); m/s for (c)-(f). The horizontal dashed lines in (a)-(b) and (e)-(f) denote south to central East China between $20°N$ and $35°N$, and the horizontal dashed lines in (c)-(d) denote the approximate northern edge of the Tibetan Plateau. The vertical dashed lines in (a)-(f) highlight June and July. Hatched area in (b), (d), (f), (g), and (h) indicates that the difference between the two categories exceeds statistical significance level at 90%.

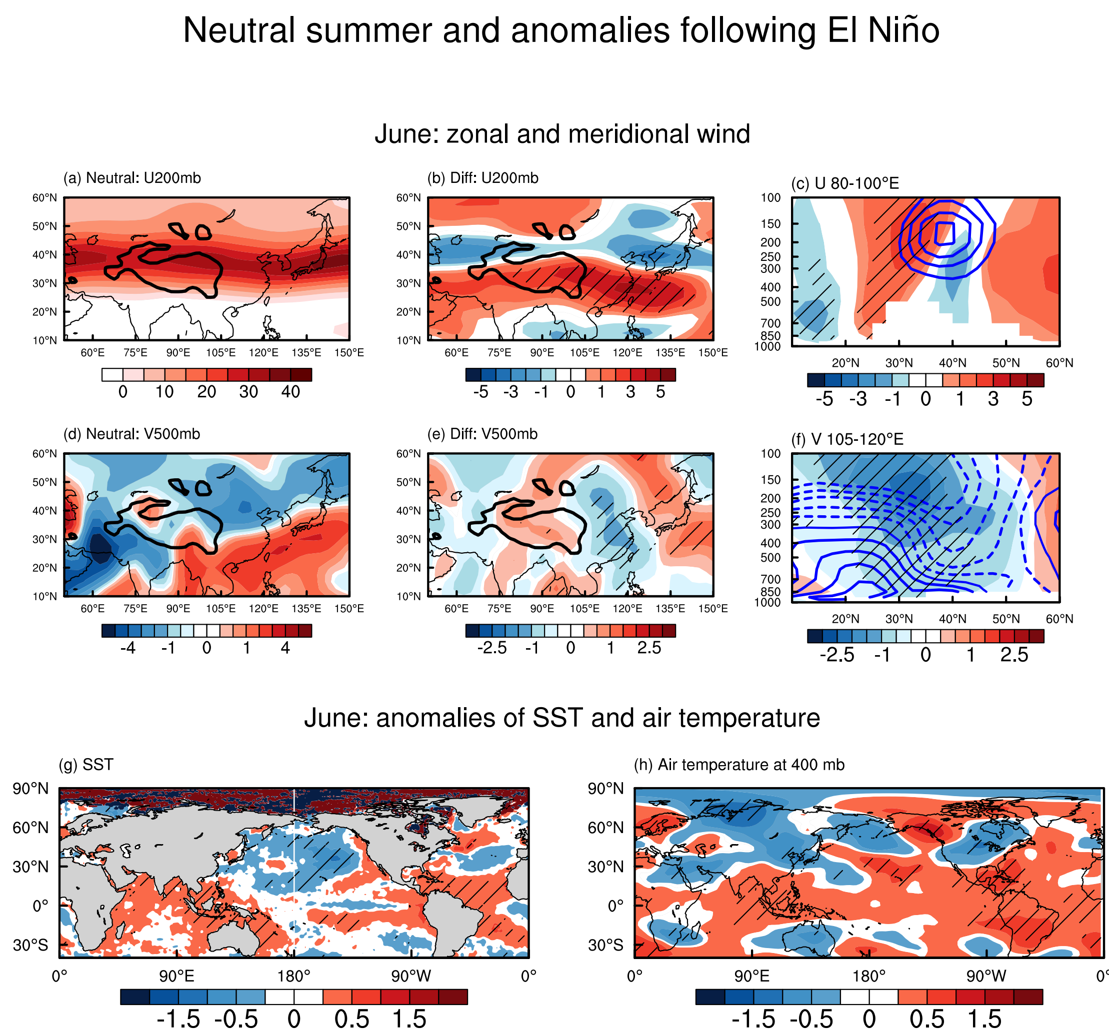

Figure 2. June zonal and meridional winds (unit: m/s), sea surface temperature (SST) and air temperature (unit: deg C). (a) 200 mb zonal winds in neutral summer, (b) anomalies of 200mb zonal wind during summers following El Niño (El Niño minus neutral summer), and (c) pressure-latitude cross section of zonal wind averaged in $80°E - 100°E$, where contours show values from neutral summer (contour interval 5 m/s), and color shading show anomalies during summers following El Niño. (d) 500mb meridional winds in neutral summer, (e) anomalies of 500mb meridonal wind during summers following El Niño, and (f) pressure-latitude cross section of meridional wind averaged in $105°E - 120°E$, where contours show values from neutral summer (negative values are dashed, contour interval 1 m/s), and color shading show anomalies during summers following El Niño. (g)-(h) Anomalies during El Niño decaying phase for (g) SST, and (h) air temperature at 400 mb. Hatched area indicates that the difference between the two categories

exceeds statistical significance level at 90%. The thick black contours in (a)-(b) and (d)-(e) indicate areas with elevation exceeding 2000 meters.

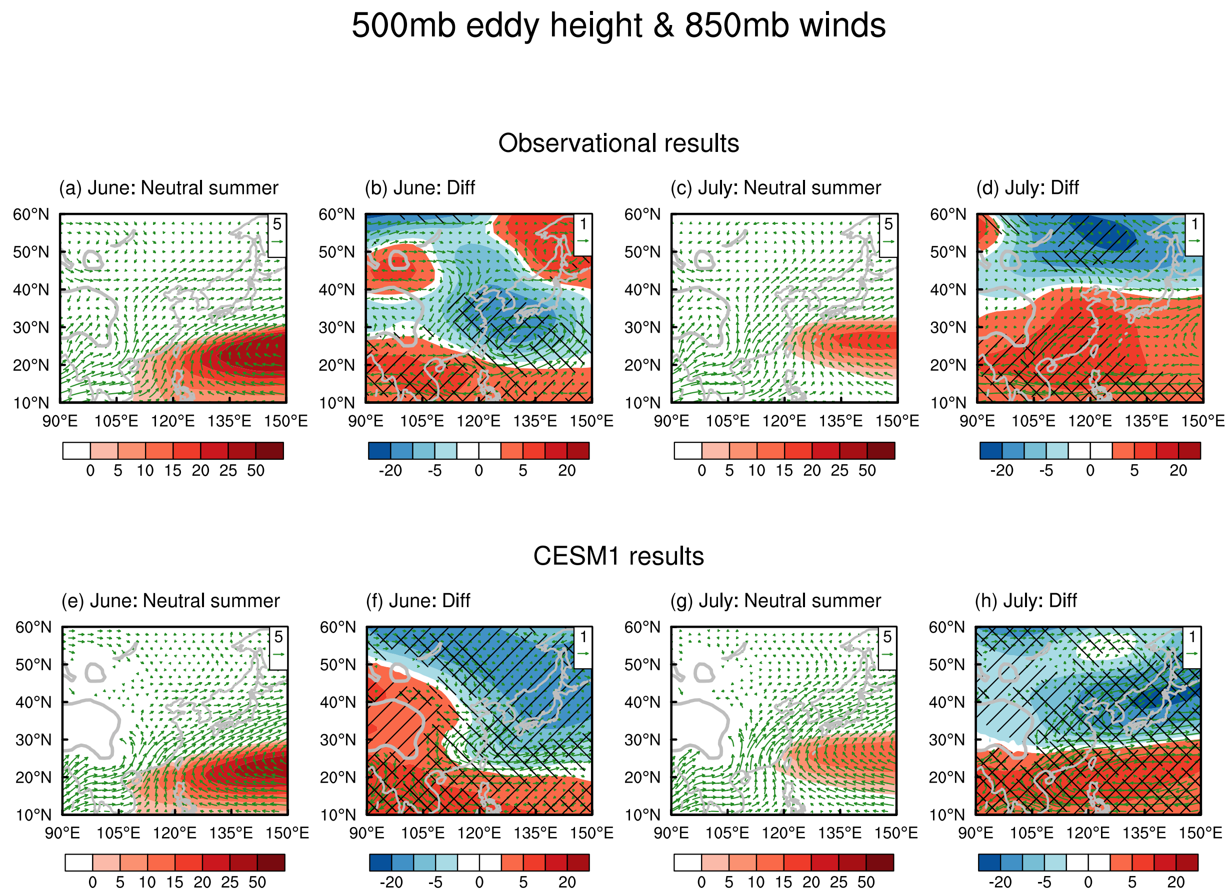

Figure 3. Eddy geopotential height at 500 mb (colors shading, unit: meters) and horizontal winds at 850 mb (green vectors, unit: m/s) from (top) observational analysis and (bottom) CESM1 control run. (a)-(b) and (e)-(f) show results in June, and (c)-(d) and (g)-(h) show results in July. Results from neutral summers are shown in (a), (c), (e), and (g). Results from anomalies during summers following El Niño are shown in (b), (d), (f), and (h). Hatched areas in (b), (d), (f), and (h) indicate that the difference exceeds statistical significance level at 90%, where the forward diagonals denote the significance for the 850 mb horizontal winds while the backward diagonals denote the

significance for the 500 mb eddy geopotential height. The thick grey contours over land indicate areas with elevation exceeding 2000 meters.

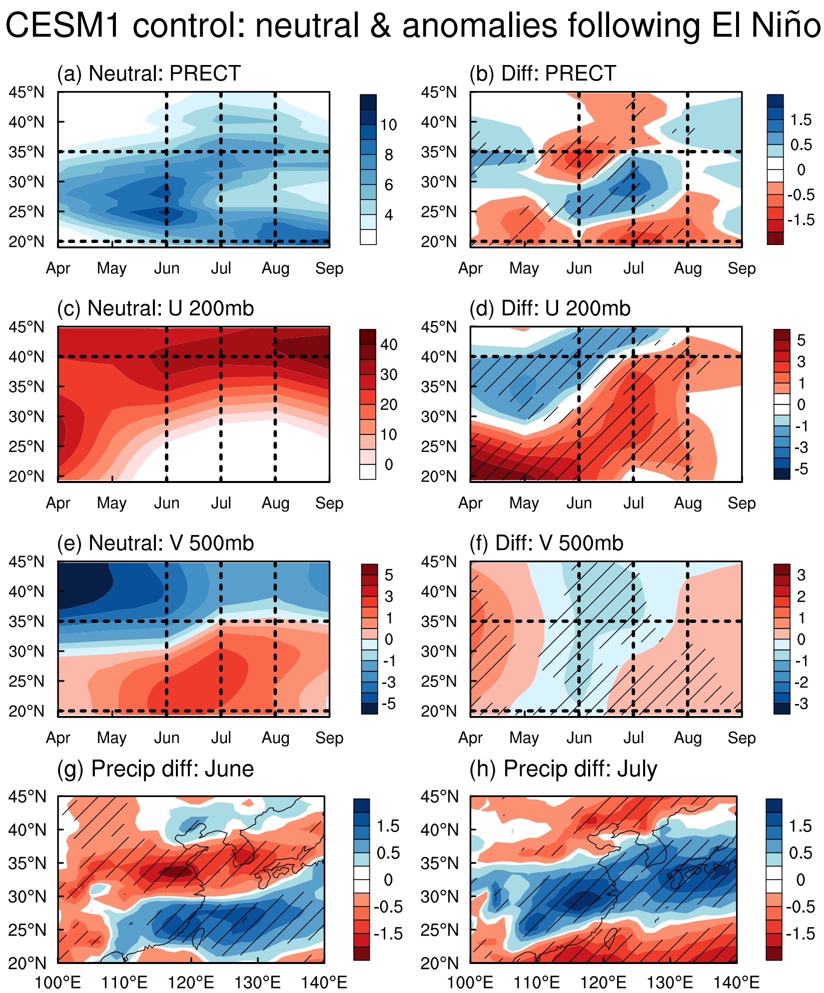

Figure 4. Total precipitation, 200 mb zonal wind, and 500 mb meridional wind from the CESM1 control run. (a)-(f) Hovmöller diagram of (a)-(b) total precipitation over East China ($105°E - 120°E$), (c)-(d) 200 mb zonal wind over the plateau region ($80°E - 100°E$), and (e)-(f) 500 mb meridional wind over East China ($105°E - 120°E$). (a), (c), (e) show results from neutral summers, and (b), (d), (f) show anomalies during summers following El Niño. (g)-(h) show precipitation anomalies during summers following El Niño for (g) June and (h) July. Unit: mm/day for (a)-(b), (g)-(h); m/s for (c)-(f). The horizontal dashed lines in (a)-(b) and (e)-(f) denote south to central East China between $20°N$ and $35°N$, and the horizontal dashed lines in (c)-(d) denote the approximate northern edge of the Tibetan Plateau. The vertical dashed lines in (a)-(f) highlight June and July. Hatched area indicates that the difference between the two categories exceeds statistical significance level at 90%.